Engineering Fracture Mechanics 149 (2015) 1–17

Contents lists available at ScienceDirect

Engineering Fracture Mechanics

journal homepage: www.elsevier.com/locate/engfracmech

The fracture mechanics of cantilever beams with an embedded sharp crack under end force loading

Xiaomin Fang, Panos G. Charalambides *

Department of Mechanical Engineering, University of Maryland, Baltimore County, Baltimore, MD 21250, USA

ARTICLE INFO

Article history:
Received 29 April 2015
Received in revised form 13 September 2015
Accepted 19 September 2015
Available online 30 September 2015

Keywords:
Linear elastic
Embedded
Sharp crack
Beam
Near-tip
Stress intensity factor
Energy release rate
Physically inadmissible

ABSTRACT

Motivated by the need to develop model and non-model based methods for damage and crack detection in components and structures, this paper aims at establishing the near-tip mechanics of cantilever beams containing a fully embedded, through thickness sharp crack and subjected to an end force. Finite element (FE) models of the cracked beams were established with the aid of a specialized 2-D adaptive meshing algorithm. Beam geometries with a crack placed at various depths and locations along the beam axis and at various orientations have been modeled. Linear elastic and isotropic conditions were assumed throughout the homogeneous beam domain. Broad parametric studies were conducted to study the effects of crack length, crack orientation and crack location on the fracture characteristics dominating both the left and right crack tips. As such extensive results are reported for the near tip energy release rates and the associated Mode I and Mode II stress intensity factors and mode mixity.

The study suggests that the near-tip conditions for both the left and right crack tips in systems with non-horizontal cracks are dominated by mixed mode conditions. Physically inadmissible crack surface interpenetrations are predicted associated with negative Mode I stress intensity factor component for at least one of the two crack tip regions for all incline cracks. The extent of crack surface interpenetration is shown to depend on the crack plane orientation relative to the beam axis.

For beams containing a horizontal crack, i.e., cracks aligned with the beam axis, the simulation results suggests that such cracks are dominated by Mode II conditions at both crack tips regardless of its length and crack location in the beam. The findings of this study along with other related results regarding the deformation of a beam with an embedded horizontal crack form the foundation for the development of analytical models capable of capturing the overall deformation as well as the near-tip fracture characteristics of such cracked structures. In addition, the findings can assist in furthering our understanding of delamination processes in laminate systems and in developing model and non-model methods for damage and crack detection.

1. Introduction

Health monitoring of mechanical components, systems and structures has received renewed attention in recent years primarily due to the aging of the infrastructure and increased use by rapid population growth. According to Doyle et al. [1],

* Corresponding author.

http://dx.doi.org/10.1016/j.engfracmech.2015.09.039
0013-7944/

Nomenclature

x, y	Cartesian coordinates
x_C, y_C	x, y coordinates of the sharp crack center
L	beam length
L_c	characteristic length
h	beam height
P	load
P_c	characteristic load
E	elastic modulus
E_c	characteristic modulus
v	Poisson's ratio
$2a$, l	crack length
$2\Delta a$, Δl	Virtual Crack Extension (VCE)
θ	crack orientation angle with respect to x-axis, counter-clockwise is positive
$\Im$	energy release rate
$\Im_c$	characteristic energy release rate
K_I	Mode I stress intensity factor (SIF)
K_{II}	Mode II stress intensity factor (SIF)
K_{ch}	characteristic SIF, as normalization factor
Ψ	mixed mode phase angle, also known as mode mixity
$\{u\}$	nodal displacement vector
N_c	number of elements participating in the implementation of the VCE method
i	elements counting index used in the VCE method
$[k_i^c]_l$	element stiffness obtained for a meshing containing a crack of length l
$[k_i^c]_{l+\Delta l}$	element stiffness obtained for a meshing containing a crack of length $l+\Delta l$

the population of the Unite States has grown from 90 million in 1900 to over 300 million in 2000. As stated in [1], over the same 100-year period, the above population growth was accompanied by a rapid expansion of the civil infrastructure building over 68,000 dams, 600,000 bridges, 530,000 miles of sewer pipes and about 3.6 million miles of surface roads. In recent years, frequent and costly infrastructure failures, such as water main breaks in major metropolitan areas, bridge aging and failures, and building collapses, have provided the impetus for the development of advance diagnostic and structural health monitoring tools.

In the past several decades, diagnosis and identification of damage in components and structures has been a field of challenging research and numerous related technical contributions have been reported. Vibration-based methods [2,3] utilizing the systems' frequency [4–7] and modal response [8,9] have been shown capable of predicting the presence of damage manifested as a local reduction in the component's structural stiffness. While these methods were shown to reliably predict the location of the damage along the beam axis, they have limited sensitivity to assess the type of damage, its extent and sub-surface location. In addition, the methods do not possess the sensitivity to differentiate between structural stiffness degradation due to modulus reduction caused for example by progressive corrosion or structural degradation caused by geometric flaws such as voids and cracks.

To address these persisting challenges, fracture mechanics concepts such as the J-integral [10] associated with the presence of sharp cracks were employed in damage detection by solving the forward problem associated with a component of given geometry and material composition containing a sharp crack of known size, orientation and crack center location. For example, Ioakimidis [11] developed a general fracture mechanics based method for nondestructive testing. In his study, he was able to locate the presence of a crack of known shape embedded in an isotropic elastic medium utilizing estimates of the path-independent J-integral. Lei [12–14] studied semi-elliptical surface cracks in plates under tension and bending utilizing the concept of J-integral and Finite Element Method (FEM).

In studying the fracture mechanics of a cracked system, the FEM has been used extensively, especially after the 1960s when progressively increased computational power became more readily available for computational research. For example, utilizing fundamental fracture mechanics concepts developed by Rice [10], Rice et al. [15] developed a finite element based stiffness derivative method in extracting from a known finite element solution the associated elastic energy release rate for a crack under Mode I conditions. Motivated by the need to understand the characteristics of fracture at bimaterial interfaces, a phenomenon prevalent in heterogeneous fiber reinforced composites and composite laminates, Charalambides et al. [16] and Matos et al. [17] extended Park's stiffness derivative method to interface cracks under mixed mode conditions. In the latter studies, they were able to establish the relative contributions of Mode I and Mode II to the mechanics of an otherwise mixed mode crack. Zhang and Charalambides [18] further improved the above methods to include interface cracks bounded by heterogeneous orthotropic media. Skrinar [19] utilized FEM to model a beam with an arbitrary number of transverse cracks. The model was then simplified such that each crack was replaced by a corresponding linear rotational spring,

connecting two adjacent elastic parts. He concluded that the method was good for the identification of cracks in beam-like structures. Potirniche et al. [20] initially introduced a 2-D damaged finite element for fracture mechanics application. Hall and Potirniche [21] extended the 2-D damaged finite element to 3-D. Using finite element method, they analyzed beam deflections and natural frequencies by testing two models: one with a user-defined element and another with an embedded edge crack. They confirmed the new element had a good potential in modeling the presence and effects of cracks. Sancho et al. [22] implemented a cohesive zone crack model in conjunction with the finite element method to analyze embedded fractures in concrete based on the strong discontinuity approach across the fracture surfaces. Their predictions were shown to match the related experimental results.

In this study, the finite element method is employed in conjunction with an adaptive 2-D meshing algorithm in modeling cantilever beams with an embedded crack and their healthy counterparts subjected to an end transverse load. As will be demonstrated later on in this study, such an integrated analysis approach enables the efficient completion of broad parametric studies needed to establish a library of forward solutions which can then be used as a database in damage detection and crack detection studies. Such database of forward solutions may include all required information needed to establish the effects of crack location, crack size and orientation on the associated fracture mechanics characteristics, i.e. the near-tip energy release rates and associated Mode I and Mode II stress intensity factors as well as information related to the deformation, slope and curvature profiles of the cracked system.

2. Finite element model description

As part of this study, an integrated mapped meshing, finite element solver and requisite post-processing algorithms are developed to model beam like structures with or without an embedded sharp crack. The goal is to conduct broad parametric studies on such structures aiming at studying the deformation response of cracked beams while also establishing the near-tip fracture characteristics for such cracked structures. Thus, parametric meshes are developed for both the healthy and cracked beams. The healthy beam geometry with dimensions, loading and displacement conditions are shown in Fig. 1a.

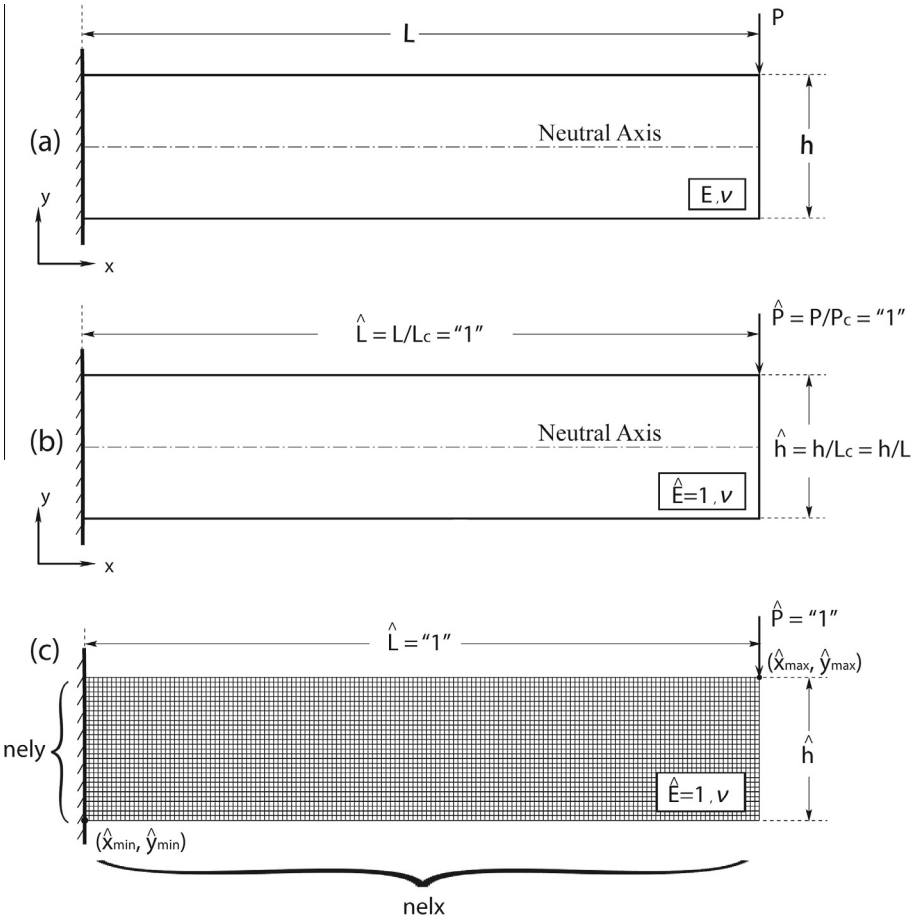

Fig. 1. (a) Healthy beam geometry with dimensions, loading and displacement conditions. (b) Healthy beam non-dimensional geometry, loading and displacement conditions. (c) A typical mesh for the healthy non-dimensional beam.

For generality purposes, the simulations reported in this study are carried out in a non-dimensional environment. Thus, the finite element mesh is developed for the non-dimensional geometry shown in Fig. 1b. Consistent with the above figure, all beam dimensions are normalized by the beams' length L which is set to be the characteristic length $L_c = L$. The loading is normalized by the characteristic load $P_c = P$, and the material modulus is normalized by the characteristic elastic modulus $E_c = E$. A typical mesh for the healthy non-dimensional beam is shown in Fig. 1c. The mesh is developed using 4-noded isoparametric elements [23]. The meshing algorithm is designed so that the mesh can be generated using only a limited number of independent variables. For example, for the healthy structure shown in Fig. 1, these variables include the x and y coordinates of the lower left and upper right corners of the beam, i.e., x_{min}, y_{min} and x_{max}, y_{max}, along with the number

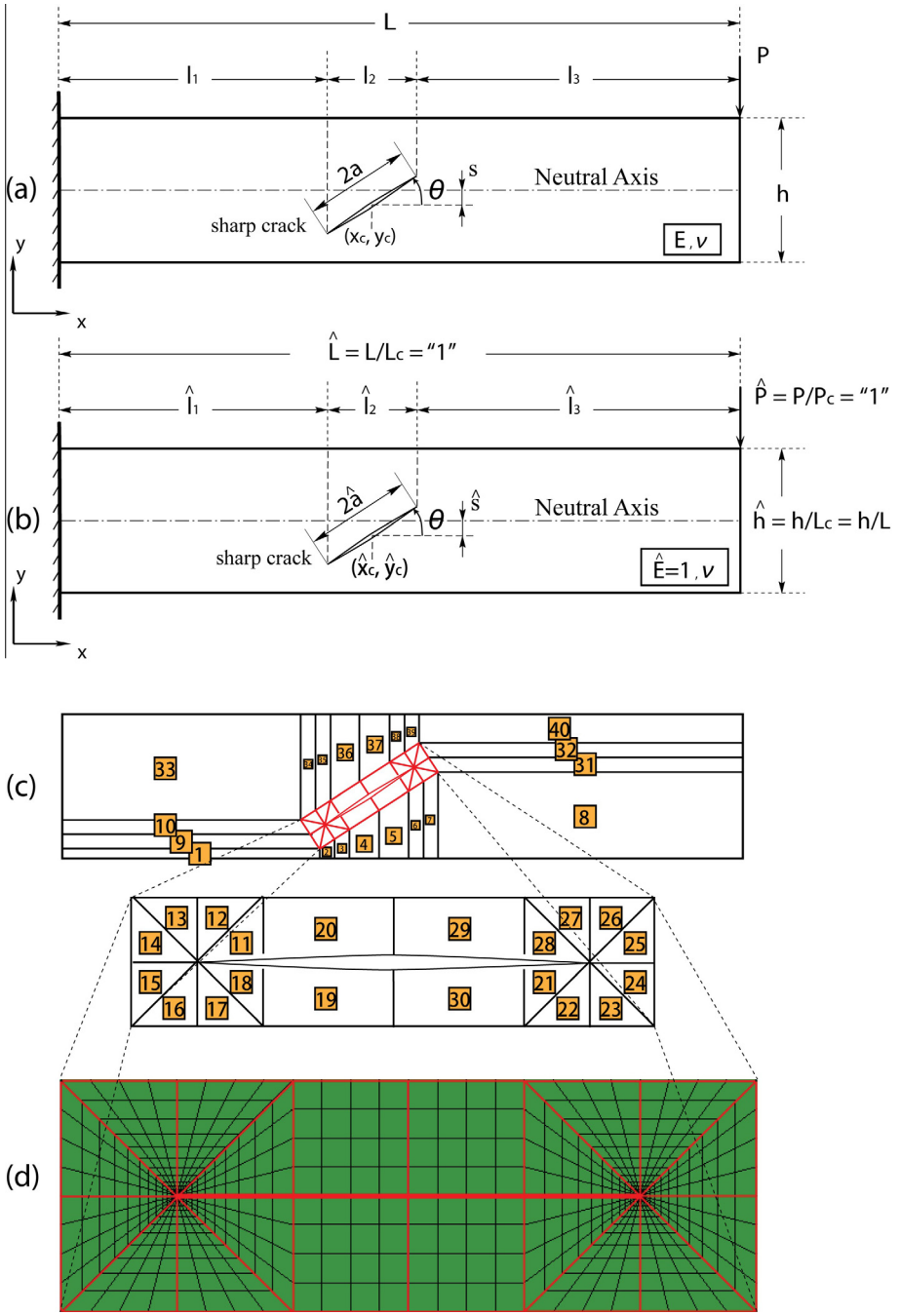

Fig. 2. (a) Cracked beam geometry with dimensions, loading and displacement conditions. (b) Cracked beam non-dimensional geometry, loading and displacement conditions. (c) Schematic of super element meshing with sub region and numbering of super elements. (d) Focused meshing scheme in the near-tip regions.

of elements *nelx* to be generated along the length of the beam or *x*-direction and the number of elements *nely* to be generated along the height of the beam or *y* direction. With the above six independent variables multiple self-similar and regular meshes can be generated. Regular meshes are used to obtain reference solutions used both in solution convergence studies as well as in comparison between the deformation characteristics of the cracked and healthy beams reported elsewhere [24].

Due to the presence of the fully embedded crack, meshing the cracked beam is a substantially more challenging task when compared to the meshing of the solid beam domain. Like the healthy beam case, the meshing algorithm is designed using a non-dimensional beam geometry. The original dimensional geometry is shown in Fig. 2a and the respective non-dimensional domain is shown in Fig. 2b. The employed non-dimensionalization follows the same process as that employed for the healthy beam. As shown in Fig. 2b, all lengths are normalized with the characteristic length which as before is taken to be the length of the beam. Accordingly, the non-dimensional crack length is taken to be the ratio of the original crack length *2a* and the beam length *L* such that $2\hat{a} = 2a/L$. In the presence of the crack, special care needs to be given to the mesh in the crack tip region. For that purpose, the domain is separated into specifically designed sub regions, each of which can then be meshed through a super element meshing approach which is discussed in greater detail in [24]. Fig. 2c highlights the selected sub regions in red and the numbering in the super element structure. Element size biased routines are developed as needed to control the element size in regions of expected high stress gradients. The focused mesh in the near-tip region is shown in Fig. 2d. Typical meshes of cracked structures comprise of approximately 6000 4-noded isoparametric elements with approximately 7000 nodes and 14,000 degrees of freedom. Sixteen rings of elements are included in each of the crack tip regions.

The material system employed is prescribed as homogeneous, linear, elastic, and isotropic, with elastic modulus E and Poisson's ratio v. In the model, the elastic modulus is non-dimensionalized by E_c as presented earlier, such that $\widehat{E} = E/E_c = 1$. The boundary conditions including both loading (the transverse end force) and boundary restraints are specified as shown in Figs. 1 and 2. The solutions for the nodal displacements were obtained by solving the finite element models associated with the healthy and cracked structures. These are then used in estimating the near-tip fracture characteristics, i.e., energy release rate and Mode I and Mode II stress intensity factors, as discussed below and in cracked-healthy beam deformation, slope and curvature comparison studies reported in [24].

3. Near-tip fracture characteristics

A through thickness planar crack fully embedded in a 2-D domain can respond to a general applied loading in one of two deformation modes also known as near-tip fracture modes [25]. Fracture Mode I is associated with loading that causes the crack surfaces to open relative to each other. Fracture Mode II on the other hand is associated with applied in-plane pure shear loading which causes the top and bottom crack surfaces to slide relative to each other. It is well established [25,26] that the linear elastic fracture fields dominating the stress, strains in the near-tip region are singular with universal spatial characteristics given by mode specific spatial eigen-functions while the intensity of the elastic fields is controlled by a mode specific single parameter known as the stress intensity factor K. Thus, in the most general cases, the near-tip fields can be fully characterized if the K_I for Mode I, K_{II} for Mode II components of the stress intensity factor (SIF) are known. If the SIF components are known, an energy quantity known as the energy release rate $\Im$ can be obtained. Importantly, $\Im$ represents the reduction of the stored elastic energy of the system with respect to crack length under displacement control conditions. The relation between SIFs and energy release rate is given through Irwin's relationship [27], i.e.,

$$\Im = \frac{1-v^2}{E}(K_I^2 + K_{II}^2) \tag{1}$$

As such, if the SIF components are known as a function of the crack characteristics, i.e. crack length, crack orientation, and crack location, one can determine the total change of elastic energy due to the introduction of the crack by integrating the energy release rate over the length of the crack.

4. Extracting the mixed mode stress intensity factors from a finite element solution

In this study, the Stiffness Derivative Method (SDM) developed by Parks [28] is employed in extracting the near-tip energy release rate from a known finite element solution. The method yields estimates of the elastic energy changes due to crack length changes by simulating a Virtual Crack Extension (VCE) [29] through a translation of the group of elements surrounding the crack tip while freezing the remainder of the mesh. In that process, a user-defined ring of elements is deformed. The changes of the element stiffness is then calculated for each element belonging to the distorted ring of elements and when coupled with the known solution of displacements at the respective element nodes, one obtains the total change of elastic energy due to the simulated Virtual Crack Extension. As such, it yields an estimate of the near-tip energy release rates as follows,

$$\Im = -\frac{1}{2}\{u\}^T \sum_{i=1}^{N_c} \frac{\partial [k_i^c]}{\partial l}\{u\} = -\frac{1}{2}\{u\}^T \sum_{i=1}^{N_c} \left\{ \frac{1}{\Delta l}([k_i^c]_{l+\Delta l} - [k_i^c]_l) \right\}\{u\} \tag{2}$$

where $[k_i^c]_l$ is the stiffness of an intra-contour element, and $[k_i^c]_{l+\Delta l}$ is the element's stiffness calculated with each of its nodes lying on near-tip contour incremented by a small extension Δl.

With the energy release rate known, the Mode I and Mode II SIF components and thus their phase angle, known as mode mixity, $\psi = \tan^{-1} K_{II}/K_I$ is then established, using the crack surface displacement (CSD) method Charalambides et al. [30] as well as the energy based method developed by Matos et al. [17] and Charalambides and Zhang [18].

5. Results and discussion

With the non-dimensional finite element model depicted in Fig. 2, the full spectrum of solutions can be explored through the following five independent non-dimensional problem parameters, i.e., the beam aspect ratio, $\hat{h} = h/L$, the normalized crack center coordinates, $\hat{x}_C = x_C/L$, $\hat{y}_C = y_C/L$, the normalized crack length $\hat{l} = l/L$ or since $l = 2a$, then $\hat{a} = a/L$, and the crack orientation angle θ. The results reported below were obtained under plane strain condition, generated through a systematic variation of individual crack parameters, i.e. crack location, crack length, and crack orientation, while fixing the beam aspect ratio.

5.1. Effects of crack location

The effects of crack location determined by the crack center coordinates $(\hat{x}_C, \hat{y}_C)$, on the near-tip mechanics are explored through systematic parametric studies wherein the beam aspect ratio is fixed at $\hat{h} = h/L = 0.2$, the crack length is fixed as $2\hat{a} = 2a/L = 0.02$, while also fixing the crack orientation angle θ to 0°, 45°, and 90°. A systematic process was employed in completing the finite element simulations in which a vertical crack was placed at one of the 231 grid locations as shown in Fig. 3. Within the rectangular domain bounded by the lower corner coordinates $(\hat{x}_C)_{min} = 0.1053$ and $(\hat{y}_C)_{min} = 0.0653$ and upper corner coordinates $(\hat{x}_C)_{max} = 0.8947$ and $(\hat{y}_C)_{max} = 0.1347$. A more detailed description of the simulation process used is presented in Ref. [24].

The results for a vertical crack, plotted in contour form within the grid domain are shown in Fig. 4 for the left or lower crack tip and Fig. 5 for the right or upper crack tip regions respectively. For the problem at hand, a contour map option was shown to be an effective method in visualizing the near-tip characteristics established through the above w parametric studies. As shown, the top left plot in Fig. 4 reports the normalized $\widehat{K}_I$ contours obtained through the parametric studies wherein vertical cracks are systematically placed within the grid domain discussed above and shown in L_c Fig. 3. For clarity purposes, the region is extracted and scaled up disproportionally in the x- and y-directions. The same format is applied in showing the contour results for the other fracture characteristics and for all three crack orientations considered, i.e. $\theta = 0^\circ,\ 45^\circ,\ 90^\circ$ reported later on in this study. Based on the non-dimensional models used, the Stress Intensity Factor (SIF) normalization factor should be $K_{ch} = P_c/L_c^{1/2}$, with P_c being a line load equal to F/w where F is the total force acting at the end of the cantilever beam and is the beam width. At the same time, the characteristics energy release rate $\Im_c = P_c^2/E_c L_c$ with E_c and being the characteristic modulus and characteristic length respectively used in non-dimensionalizing each finite element model. It is note-worthy that in order to avoid any confusion with the notation used to denote the material toughness K_{Ic} or K_c, the SIF normalization factor is labeled to K_{ch}, with the "ch" subscript denoting "Characteristic" quantity.

It is of interest to observe that the non-dimensional $\widehat{K}_I$ contours shown in the upper left plot in Fig. 4 vary from a minimum of approximately −8 at the lower left corner to a maximum of +5 at the upper left corner of the parametric domain. Thus, a $\widehat{K}_I = 0$ line exists above which the left or lower crack tip is shown to be dominated by a positive Mode I component associated with or physically admissible crack opening conditions. Thus, the left or lower crack tip is associated with a positive $\widehat{K}_I$ for cracks centered above the thick black line shown in the plot which implies that the left crack tip for those systems remains open. On the contrary, for cracks placed below the line, the Mode I component $\widehat{K}_I$ is predicted to be

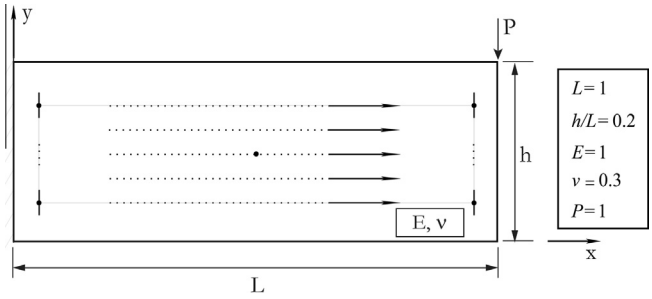

Fig. 3. Schematic of parametric study on the effects of crack location on the fracture characteristics with fixed beam aspect ratio, crack orientation, and crack length. The crack location varies at the grid points which form a rectangular area inside the domain. The five black dots highlight both the four corners of the rectangular area and the domain center. The rectangular area is symmetric about the domain center. The results reported in Figs. 4–9 were obtained under plane strain condition.

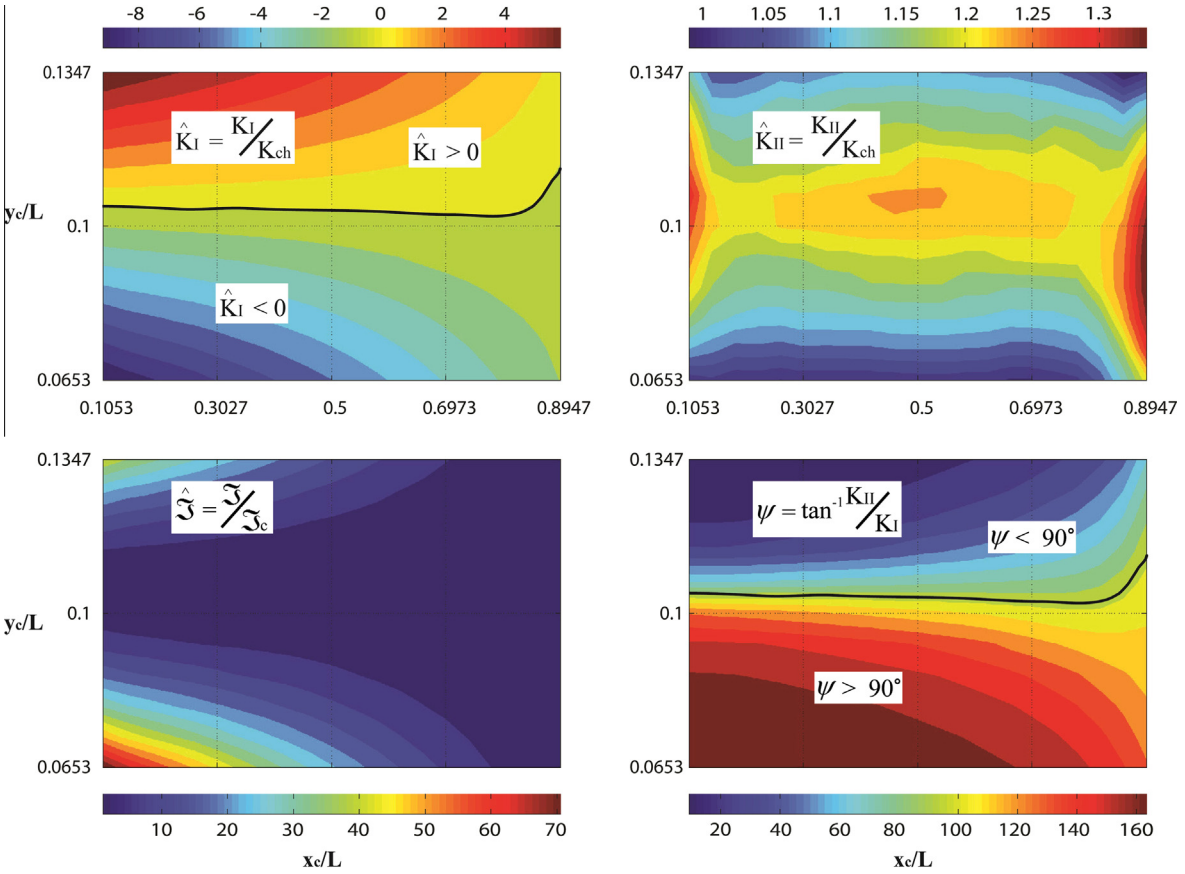

Fig. 4. Contour plots of the non-dimensional near-tip fracture characteristics obtained under plane strain condition, such as energy release rate, Mode I and Mode II stress intensity factors (SIFs), and phase angle at the left crack tip of the cracked beam, with various crack location. The contours were obtained by placing a vertical crack within a rectangular grid region shown in Fig. 3. The beam aspect ratio is $h/L = 0.2$, crack orientation $\theta = 90^\circ$, and crack length $l/L = 2a/L = 0.02$. Crack closure in the left crack tip region, i.e., lower crack tip for cracks placed below the line of $\widehat{K}_I = 0$ which also corresponds to $\Psi > 90^\circ$ as shown in the contour of phase angle.

negative which is physically inadmissible. This implies that for the latter systems, crack closure is predicted in the lower crack-tip region. A physically admissible solution for such systems will require solving a non-linear problem that accounts for crack surfaces contact during deformation. Such effects have been addressed elsewhere [24] and were shown to have minimal effects on the near-tip mechanics of the other crack tip which was predicted by the linear theory to undergo physically admissible crack surface opening and relative sliding conditions.

Contour of the Mode II component of the stress intensity factor is shown in the top right plot in Fig. 4. The non-dimensional $\widehat{K}_{II}$ levels are indicated by the color bar above the plot. As shown, vertical cracks placed in a cantilever beam systems under an end force loading experience appreciable amount of relative crack surface sliding as measured by the Mode II component of the stress intensity factor. As expected, the direction of relative crack surface sliding is shown to be consistent with the positive sign of the $\widehat{K}_{II}$ component and the transverse shear directions induced by the applied downward force. Negative values of $\widehat{K}_I$ along with positive $\widehat{K}_{II}$ values give rise to the mode mixity $\Psi > 90^\circ$. As such, the crack closure effects predicted through the $\widehat{K}_I < 0$ contours are also predicted through the $\Psi > 90^\circ$ contour region shown in the right lower plot in Fig. 4. While one may be inclined to ignore all results associated with physically inadmissible $\widehat{K}_I < 0$ values, the above results which are included in Fig. 4 and all subsequent figures may still be of relevance. More specifically, the reported results were obtained for the case of a downward pointing load P. However, the same results may become relevant for an upward pointing load P while in the latter case the reported positive $\widehat{K}_I$ results also reverse sign and become irrelevant.

In Fig. 4, the lower left contour plot shows the normalized energy release rate made available to the left or lower crack tip, i.e., the crack tip located below a horizontal line passing through the crack center. The level of available energy is indicated by the color bar below the plot. As shown, maximum energy is made available to the lower crack tip for beams containing a vertical crack centered at the lower left corner of the referenced region. However, given the high contribution to the energy release rate from a physically inadmissible $\widehat{K}_I$ as discussed above, the energy release rate values below the $\widehat{K}_I = 0$ line reported in this study ought to be discounted. However, the corresponding contours above the $\widehat{K}_I = 0$ line remain valid since

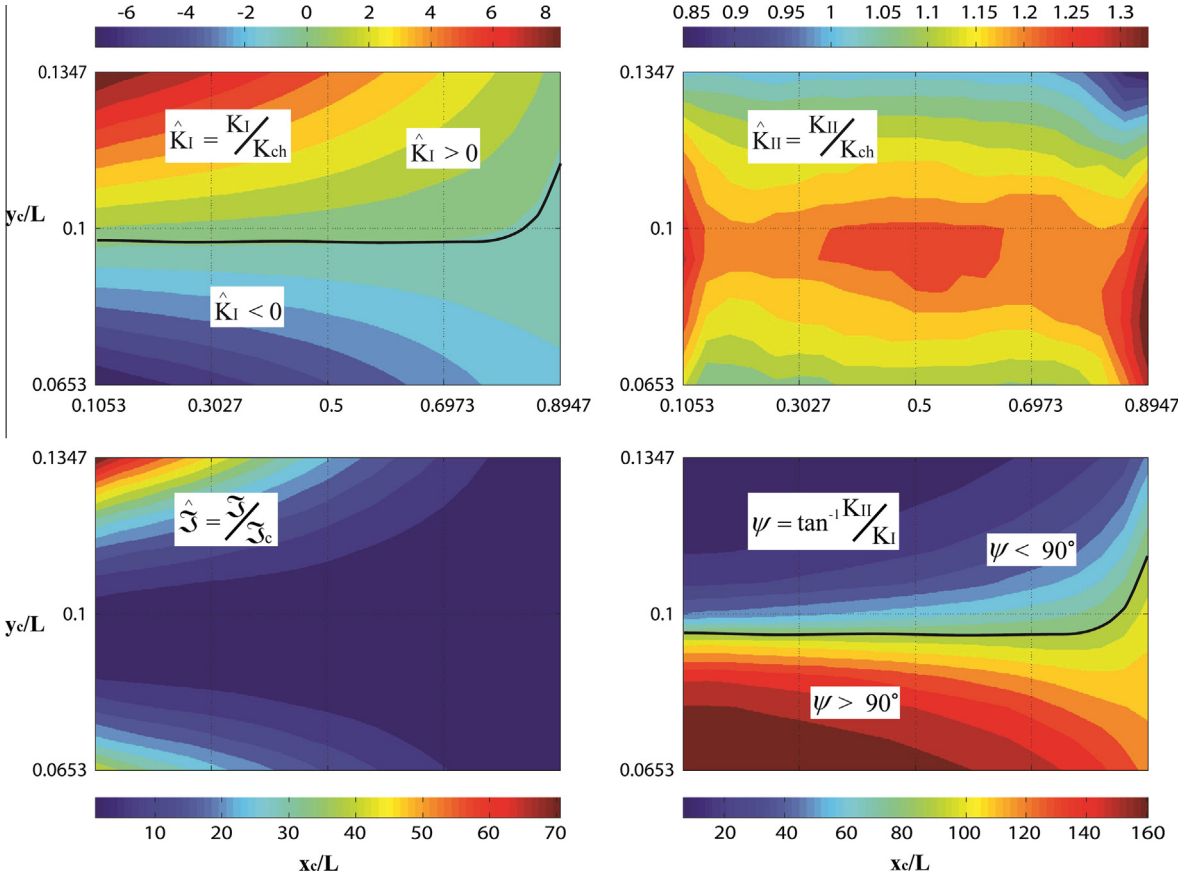

Fig. 5. Right crack-tip contour plots of the non-dimensional near-tip energy release rate, Mode I and Mode II stress intensity factors, and associated phase angle, obtained under plane strain condition. As in Fig. 4, the contours are obtained by placing a vertical crack within a rectangular grid region as shown in Fig. 3. The beam geometry and crack characteristics are those given in Fig. 4. Crack closure in the left crack tip region, i.e., upper crack tip, is predicted for cracks placed below the line of $\hat{K}_I = 0$ which also corresponds to $\Psi > 90^\circ$ as shown in the Ψ contour plot.

for those systems both the left and right crack tips remain open. As such, a maximum value for the energy release rate is predicted for systems with a vertical crack at the upper left corner of the parametric studies domain. This is indeed expected since that region is subjected to high tensile stresses due to bending.

Similar results to those reported in Fig. 4 for the near-tip fracture characteristics for the right or upper crack tip region are shown in Fig. 5. At a first glance, all plots for the right or upper crack tip region appear to exhibit similar trends to their counterparts shown in Fig. 4 for the left or lower crack tip region. However, and as expected since the upper crack tip region is embedded within a region of higher tensile bending stress compared to the lower crack tip, higher values are predicted for the available energy release rate and Mode I SIF component when compared to those for the left or lower crack tip. Crack closure is predicted for the right or upper tip region for beam systems containing a crack placed below the heavy line shown in the $\widehat{K}_I$ plot at the top left corner in Fig. 5.

Given the specified crack length of $2\hat{a} = 2a/L = 0.02$, and in light of the predictions reported in Figs. 4 and 5, one can conclude that when a vertical crack is placed entirely within the compressive bending region with its center slightly below the beam neutral axis, the crack will remain close during the application of a downward load although relative crack surface sliding is predicted at both crack tips due to a non-zero mode II component. The same crack however is expected to totally open if the direction of loading was to be reversed. Such findings may provide useful insights on the development of related beam models for frequency and modal analysis of vibrating beams containing such a crack.

Results similar to those reported in Figs. 4 and 5 for the left and right crack tip respectively are also presented for $\theta = 0^\circ$ and $\theta = 45^\circ$ in Figs. 6–9. The beam aspect ratio used in these studies is $h/L = 0.2$ whereas the crack length is $l/L = 2a/L = 0.02$. More specifically, Fig. 6 reports on contour maps for the Mode I and Mode II stress intensity factor components, their mode mixity, and the associated energy release rate in the left crack tip region of a crack of $\theta = 45^\circ$. As shown, substantial regions exist wherein the Mode I stress intensity factor is negative. As discussed earlier, negative $\widehat{K}_I$ values are physically not admissible and they are the result of using linear theory allowing crack surface interpenetration in the current study. In regions of positive $\widehat{K}_I$, it is also shown that a healthy $\widehat{K}_{II}$ component exists, which implies that in most instances the left crack tip is subjected to mixed mode conditions. The mode mixity as well as the energy release rate made available to the

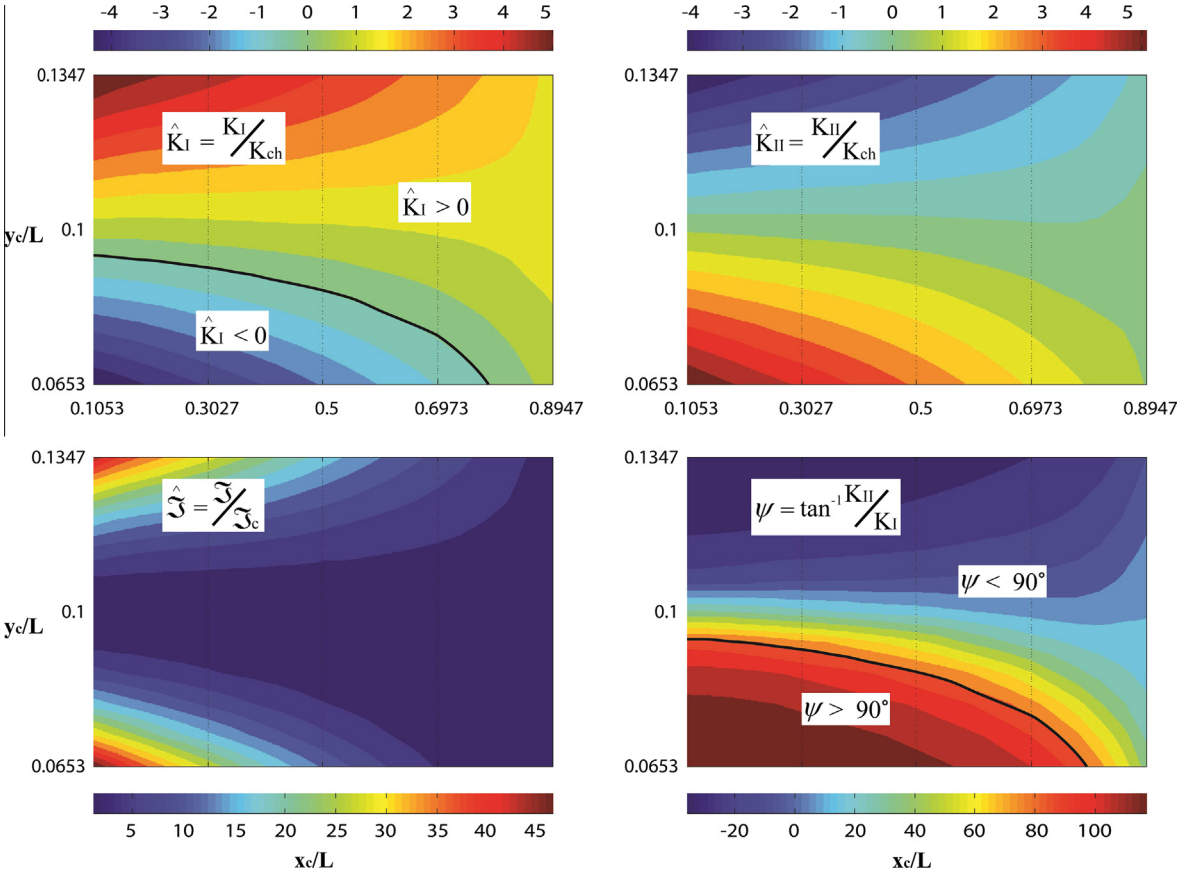

Fig. 6. Contour plots of the non-dimensional near-tip fracture characteristics obtained under plane strain condition, such as energy release rate, Mode I and Mode II stress intensity factors (SIFs), and phase angle at the left crack tip of the cracked beam, with various crack location. The contours were obtained by placing a crack of orientation angle $\theta = 45^\circ$ within a rectangular grid region as shown in Fig. 3. The beam aspect ratio is $h/L = 0.2$ and crack length $l/L = 2a/L = 0.02$. According to the plots of Mode I and Mode II SIF components, the mixed mode condition dominates the solution domain.

left crack tip are also shown in Fig. 6. Again, for systems with a crack predicted to experience crack surface closure, i.e., $\widehat{K}_I < 0$, the reported energy release rate predicted ought to be discounted. The contour plots for the near tip fracture characteristics dominating the right crack tip region are shown in Fig. 7.

As shown in Figs. 6 and 7, both the left and right crack tip regions are dominated by mixed mode conditions. Most specifically, the mode mixity Ψ appears to be in the range of -20° to 80° for the majority of the solution domain. Regions of crack closure are also predicted for the crack tip regions as reflected through the contours shown in the top left plots of Figs. 6 and 7. Again a healthy Mode II component exists throughout the reference domain as shown in the $\widehat{K}_{II}$ contour plots at the top right corner in Figs. 6 and 7.

The plots of fracture characteristics for a horizontal crack, i.e., $\theta = 0^\circ$, are presented in Fig. 8 for the left crack tip and Fig. 9 for the right crack tip. It is of profound interest to observe that the $\widehat{K}_I$ contours suggest that the corresponding $\widehat{K}_I$ component for both the left and right crack tip regions is very close to zero, while a healthy Mode II component exist throughout the solution domain for both crack tips. Clearly, the above observation does not apply to the end beam region due to the end effects induced by the application of the end concentrated force. As shown in Figs. 8 and 9, a small but noticeable positive $\widehat{K}_I$ values appear to exist in the lower left corner of the simulation region. These small regions of slightly positive $\widehat{K}_I$ appear in the contour plots reported in Fig. 8 for the left crack tip and Fig. 9 for the right crack tip. As shown, the positive $\widehat{K}_I$ contours in Fig. 9 for the right tip appear to be a little more extensive compared to those of the left tip reported in Fig. 8. As discussed above, the results shown in the above figures provide strong evidence that a horizontal crack placed away from the beam ends anywhere in the interior of the beam is dominated by Mode II conditions. The positive $\widehat{K}_I$ regions predicted for cracks placed at the lower corner of the simulation region may suggest that local deformation mechanisms such as micro-buckling of the beam regions above and below the crack subjected to compressive bending stresses may play some role in determining the deformation and fracture mechanics conditions for such cracks. For example, under Mode II conditions, relative in-plane crack surface sliding takes place. However, for horizontal cracks placed in the vicinity of the fixed end in the compressive region, the in-plane crack surface sliding is constrained by the zero displacement condition at the fixed

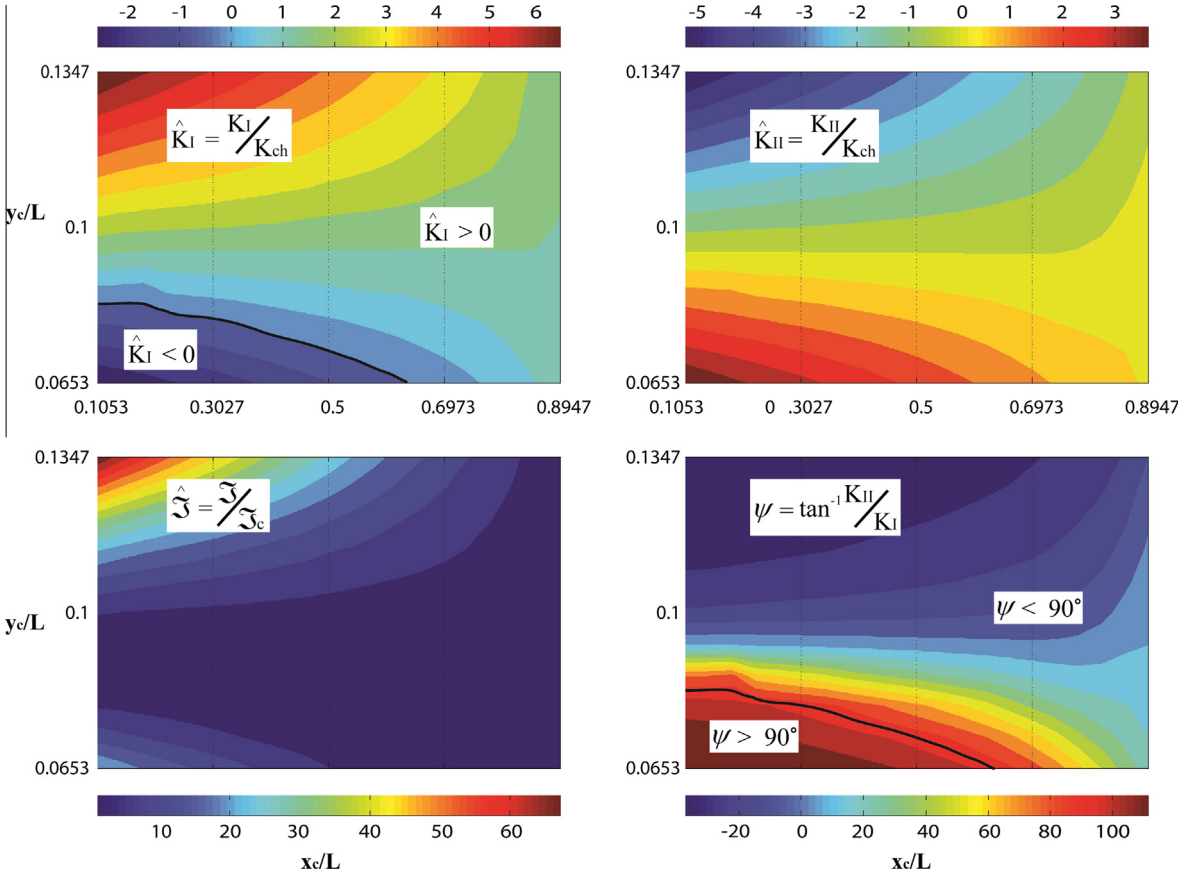

Fig. 7. Contour plots of the non-dimensional near-tip fracture characteristics obtained under plane strain condition, such as energy release rate, Mode I and Mode II stress intensity factors (SIFs), and phase angle at the right crack tip of the cracked beam, with various crack location. The contours were obtained by placing a crack of orientation angle $\theta = 45^\circ$ within a rectangular grid region as shown in Fig. 3. The beam geometry and crack characteristics are same as those given in Fig. 6. According to the plots of Mode I and Mode II SIF components, the mixed mode condition dominates the solution domain.

end. As a result, the beam area below the horizontal crack that resides within the high compressive bending region may experience micro-buckling giving rise to a slight positive Mode I component as predicted via the finite element simulations reported in Figs. 8 and 9.

The above observation suggests that a horizontal crack embedded in a cantilever beam under an end force condition behaves more like a pure Mode II crack. Simulation results reported elsewhere [24] show that the Mode II dominance applies not only to the short stubby beams, such as of aspect ratio $h/L = 0.2$, but also to the slender beams, such as of aspect ratio $h/L = 0.1$ and 0.05. In fact, this observation is utilized in parallel studies [24], wherein the effects of the crack on the deformation, slope, and curvature characteristics for beams containing horizontal cracks are investigated. In addition, the observation lays the foundation for the development of relevant analytical models capable of predicting the mechanical and fracture response of beams with embedded horizontal cracks.

5.2. Effects of crack length

In this section, the relation between the near-tip fracture characteristics and crack length will be studied. In the proposed parametric study, the beam aspect ratio is fixed at $h/L = 0.2$, the crack location is fixed at the center of the rectangular domain at normalized coordinates $(\hat{x}_C, \hat{y}_C) = (0.5, 0.1)$. Parametric studies varying the normalized crack length are carried out for five different crack orientations, i.e. $\theta = -90^\circ,\ -45^\circ,\ 0^\circ,\ 45^\circ,\ 90^\circ$. In each case, the crack length is systematically varied within the range of $l/L = [0.03, 0.12]$, with its center fixed at the beam domain center. For each crack orientation, the parametric study initiates with a normalized crack length $l/L = 2a/L = 0.03$, and ends with $l/L = 2a/L = 0.12$. A symmetrically imposed crack length increment of $\Delta\hat{l} = 2\Delta\hat{a} = 0.005$ is used resulting in 19 different cracked beam models for each simulation run. Fig. 10 shows a schematic wherein the crack is placed at the beam center and for each crack angle the crack is allowed to increase its simulation length symmetrically within the crack length range specified above. For clarity purposes, it may be of importance to note that the results reported in Fig. 11 are for the left crack tip whereas those reported in Fig. 12 are for the right crack tip. The cases reported for $\theta = 90^\circ$ and $\theta = -90^\circ$ model the same vertical crack configuration. For

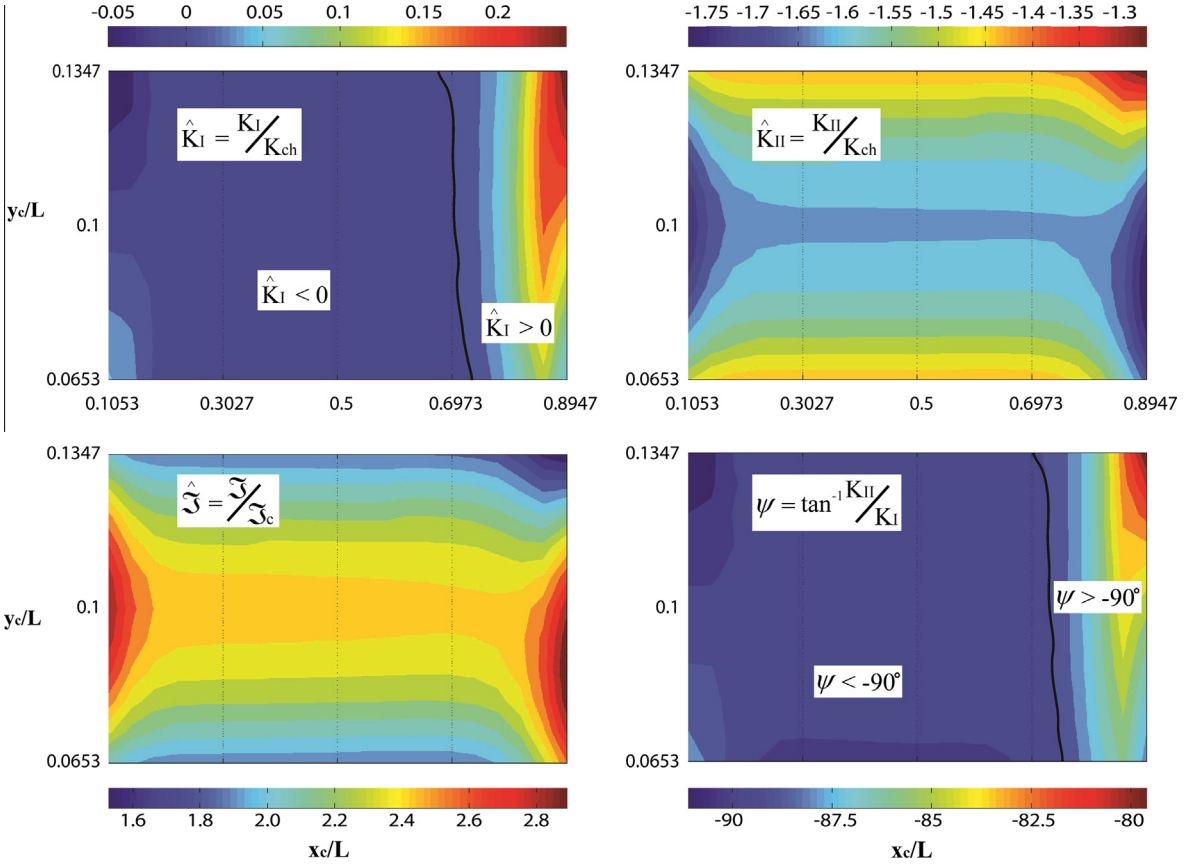

Fig. 8. Contour plots of the non-dimensional near-tip fracture characteristics obtained under plane strain condition, such as energy release rate, Mode I and Mode II stress intensity factors (SIFs), and phase angle at the left crack tip of the cracked beam, with various crack location. The contours were obtained by placing a horizontal crack within a rectangular grid region as shown in Fig. 3. The beam aspect ratio is $h/L = 0.2$, crack orientation is $\theta = 0°$, and crack length is $l/L = 2a/L = 0.02$. Mode II component $\hat{K}_{II}$ dominates the solution domain, while $\hat{K}_I$ is close to 0.

$\theta = 90°$, the left crack tip is the lower tip whereas for $\theta = -90°$, the left crack tip is the upper tip. Similarly, for $\theta = 90°$, the right crack tip is the upper tip whereas for $\theta = -90°$, it is the lower tip. One then recognizes that both figures report the same results for the lower and upper tip for a vertical crack no matter whether is modeled using $\theta = 90°$ or $\theta = -90°$.

Fig. 11 shows the simulation predictions for the normalized energy release rate, the normalized Mode I and Mode II stress intensity factors as well for their phase angle Ψ. In each plot, the simulation predictions are shown using discrete points whereas the lines represent a graphical interpolation between points. The points and curve in yellow, blue, black, green, and red correspond to crack orientation $\theta = -90°,\ -45°,\ 0°,\ 45°,\ 90°$, respectively.

As shown in Fig. 11, the energy release rate (see bottom left plot) at the left crack tip for $\theta = +45°$ (in green) coincides with the left tip predictions for a crack oriented at $\theta = -45°$ (in blue). The same feature is exhibited by the energy release rate curves at $\theta = \pm 90°$ (in yellow and red respectively). In addition, the results suggest that the energy release rate increases monotonically with crack length for all cases considered. As shown, when the crack is vertical and the left crack tip is placed in the tensile bending region above the neutral axis, i.e. $\theta = -90°$, appreciably higher levels of the energy release rate are made available to the crack tip when compared to all other crack orientations considered.

Of interest are the normalized $\hat{K}_I$ profiles shown in Fig. 11. Recall that a positive $\hat{K}_I$ implies that the respective crack tip region opens up during loading whereas a negative $\hat{K}_I$ value implies crack closure as the crack surface come into contact during loading. Of the reported curves, at the left crack tip, only the cracks of $\theta = -90°$ and $\theta = +45°$ show a positive Mode I component. In fact, for the orientation of $\theta = -90°$, the left crack tip is above the neutral axis in an area subjected to moderate tension due to bending. On the contrary, when $\theta = +90°$, the left crack tip resides with a moderately compressive stress region below the beam's neutral axis resulting in a physically inadmissible negative Mode I SIF component. For the orientations of $\theta = \pm 45°$, the left crack tip experiences a more complicate mixed mode condition.

It is also of interest to observe that for a horizontal crack, i.e., $\theta = 0°$, the Mode I stress intensity factor component is predicted to be negligible, i.e. $\hat{K}_I = 0$. However, the Mode II component is not negligible, i.e. $\hat{K}_{II} \neq 0$. Such a crack would behave as if a pure Mode II crack with in-plane crack surface sliding dominating the near-tip mechanics of both the left and right crack-tip regions as will be demonstrated below. Supported by the contour figures presented earlier in this work,

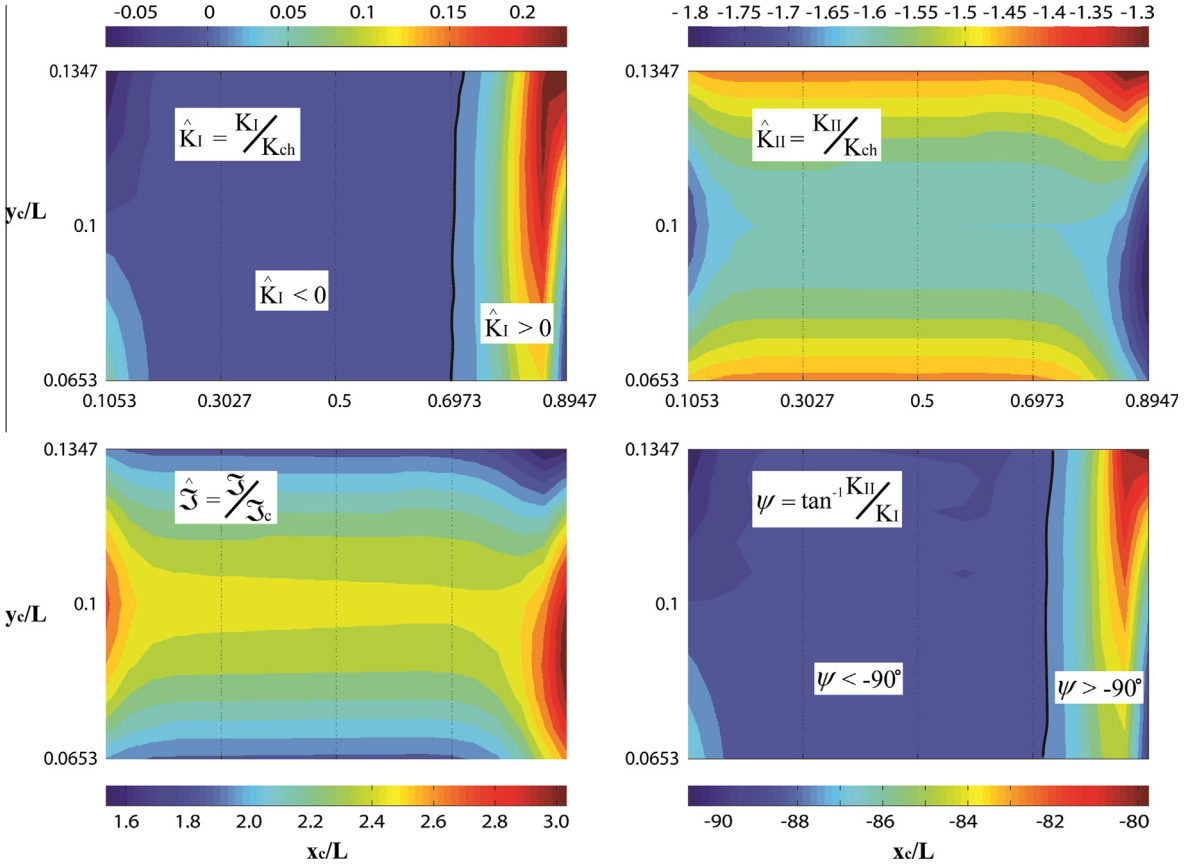

Fig. 9. Contour plots of the non-dimensional near-tip fracture characteristics obtained under plane strain condition, such as energy release rate, Mode I and Mode II stress intensity factors (SIFs), and phase angle at the right crack tip of the cracked beam, with various crack location. The contours were obtained by placing a horizontal crack within a rectangular grid region as shown in Fig. 3. The beam geometry and crack characteristics are same as those given in Fig. 8. Mode II component $\hat{K}_{II}$ dominates the solution domain, while $\hat{K}_I$ is close to 0.

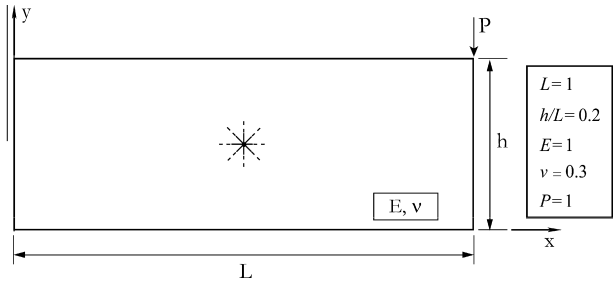

Fig. 10. Schematic showing a crack placed at the beam center at five different orientations, i.e. $\theta = -90°,\ -45°,\ 0°,\ 45°,\ 90°$. The dash lines at each crack tip indicate that in this simulation, cracks of varying length are modeled with each case having the crack center located at the beam domain center and the crack placed symmetrically with respect to the crack surface normal passing through the beam domain center. The results reported in Figs. 11 and 12 were obtained under plane strain condition.

this finding appears to hold true regardless of the depth at which the horizontal crack is placed and forms the basis for the development of related analytical solutions for the near-tip mechanics of such horizontally placed cracks.

The $\widehat{K}_{II}$ profiles plotted against the normalized crack length for the five crack orientation angles considered above and shown in Fig. 11, suggest that for most crack configurations and crack lengths considered in these simulations, the Mode II SIF component is not zero and appears to play a major role in determining the near-tip mechanics for the left crack tip and as will be seen later on for its right counterpart as well. It is notable that of all crack configurations considered in obtaining the results reported in Fig. 11 (i.e. crack lengths and crack orientations), and with the exception of the case of a horizontal crack, i.e., $\theta = 0°$, not other configuration is predicted to experience a pure Mode II condition at the left or right crack tips (see also Fig. 12). In most instances, mixed mode conditions dominate the near-tip regions.

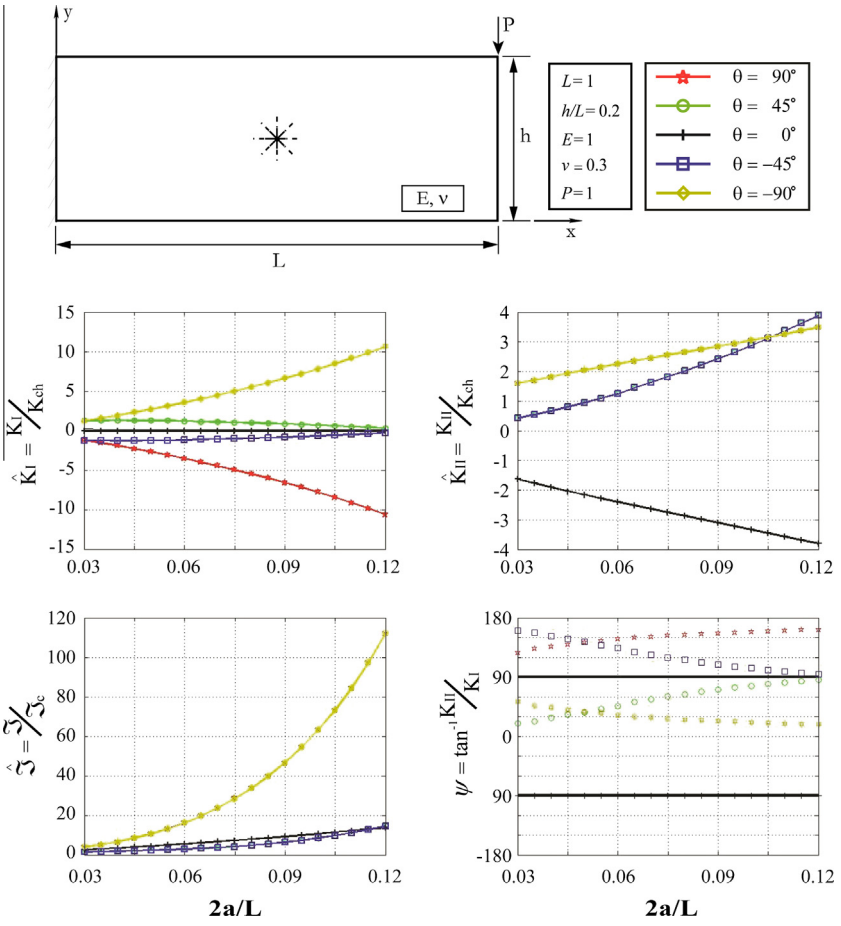

Fig. 11. The normalized left crack tip fracture characteristics such as the energy release rate, the Mode I and Mode II stress intensity factors (SIFs), and mode mixity are plotted against the non-dimensional crack length $\hat{l} = l/L = 2a/L$. The normalized crack length is varied from 0.03 to 0.12 with increment $\Delta\hat{l} = 2\Delta\hat{a} = 0.005$. The five different curves represent the results for five different crack orientations, i.e. $\theta = -90^\circ,\ -45^\circ,\ 0^\circ,\ 45^\circ,\ 90^\circ$. The energy release rate and Mode II SIF results for $\theta = -90^\circ$ (in yellow) coincide with those of $\theta = +90^\circ$ (in red), and the curves and/or points of $\theta = -45^\circ$ (in blue) coincide with those of $\theta = +45^\circ$ (in green). All results were obtained under plane strain condition. (For interpretation of the references to color in this figure legend, the reader is referred to the web version of this article.)

The results on the normalized near-tip fracture characteristics for the right crack tip are reported in Fig. 12 in a manner similar to that used in reporting the results in Fig. 11. Overall, the trends in the energy release rate, Mode I and Mode II SIFs and their phase angle reported in Fig. 12 appear to be similar to those reported in Fig. 11 for the left crack tip. For example, the energy release rate profiles at the right crack tip for cracks oriented at $\theta = +45^\circ$ (in green) are predicted to coincide with those obtained for a crack oriented at $\theta = -45^\circ$ (in blue). Similarly, and consistent with the results reported in Fig. 11, the energy release rate profiles for cracks oriented at $\theta = \pm 90^\circ$ are also predicted to coincide. The overall values of the non-dimensional energy release rate made available to the right crack tip also appear to be in parity with their left crack tip counterparts for $\theta = \pm 90^\circ,\ 0^\circ$, but are slightly different for $\theta = \pm 45^\circ$ with the right tip energy release rates shown to be higher than those made available to the left tip. Another difference between the right and left crack tip fracture characteristics exists between the $\widehat{K}_I$ trends shown in Fig. 11 for the left crack tip for cracks oriented at $\theta = \pm 45^\circ$ and the corresponding trends for the right tip shown in Fig. 12. More specifically, Fig. 11 shows that at the left crack tip, for cracks oriented at $\theta = +45^\circ$, $\widehat{K}_I$ decreases with increasing crack length whereas at the right tip it is shown to increase. This does make sense since for a crack oriented at $\theta = +45^\circ$, the left crack tip "grows" increasingly into a compressive stress regime whereas the right tip "grows" into an increasingly tensile stress region. For a crack oriented at $\theta = -45^\circ$, the reverse applies, i.e. the left tip is above the neutral axis and "grows" into increasingly higher tensile stress region whereas the right tip is placed below the beam neutral axis and in a region subjected to increasing compressive bending stress with increasing crack length. Consistent with the above observation, $\widehat{K}_I$ is shown to increase with crack length at the left crack tip (see Fig. 11), whereas it is shown to decrease at the right tip, albeit into a more negative and physically inadmissible regime.

Consistent with the results reported in Fig. 11 for the left crack tip, the results reported in Fig. 12 for the right tip also suggests that an appreciable component of Mode II does exist at the right tip for all orientations considered. In the special

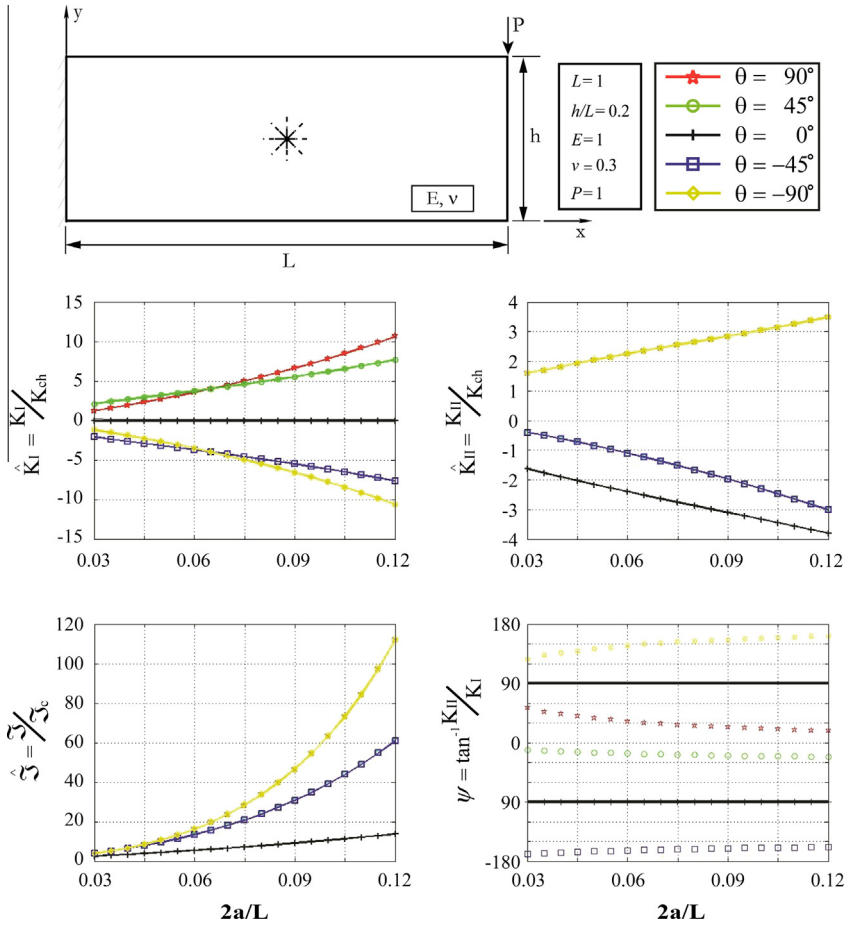

Fig. 12. The normalized right crack tip energy release rate, Mode I and Mode II stress intensity factors (SIFs), and mode mixity, obtained under plane strain condition, are plotted against the non-dimensional crack length $\hat{l} = l/L = 2a/L$. The normalized crack length is varied from 0.03 to 0.12 with increment $\Delta\hat{l} = 2\Delta\hat{a} = 0.005$. The five different curves represent results for five different crack orientations, i.e. $\theta = -90^\circ,\ -45^\circ,\ 0^\circ,\ 45^\circ,\ 90^\circ$. The energy release rate and Mode II SIF results for $\theta = -90^\circ$ (in yellow) coincide with those of $\theta = +90^\circ$ (in red), and the curves and/or points of $\theta = -45^\circ$ (in blue) coincide with those of $\theta = +45^\circ$ (in green). (For interpretation of the references to color in this figure legend, the reader is referred to the web version of this article.)

case of a horizontal crack, the Mode II component dominates in both the left and right crack tip regions suggesting that a fully embedded horizontal crack is behaving more like a pure Mode II crack. For all other crack orientations considered, the results suggest that the right crack tip, like the left, is subjected to mixed mode fracture conditions.

5.3. Effects of crack orientation

In this section, the relation between the fracture characteristics and crack orientation, measured counter clockwise as positive from positive x direction is studied using yet another parametric study. In the proposed parametric study, as before, the beam aspect ratio is fixed at $h/l = 0.2$, the crack location is fixed at the center of the rectangular domain, i.e. $(\hat{x}_C, \hat{y}_C) = (0.5, 0.1)$. The parametric studies are conducted for four different normalized crack lengths, i.e. $l/L = 0.03,\ 0.05,\ 0.07,\ 0.10$ or $a/L = 0.015,\ 0.025,\ 0.035,\ 0.05$. The crack orientation is varied in the range of $[-90^\circ, +90^\circ]$. For each crack length considered, the first model is formulated for a crack oriented at -90° and for each subsequent model the crack orientation is increased by an increment of $+5^\circ$, which results in a total of 37 models. Fig. 13 shows the fundamental parameters involved in the crack orientation parametric study.

Figs. 14 and 15 show the parametric study results for the left and right tips respectively. As in Figs. 11, 12, 14 and 15 include plots for the normalized near tip energy release rate, the Mode I and Mode II stress intensity factors and their phase angle used to measure the mode mixity. Initial focus is placed on the profiles of the Mode I SIF component $\widehat{K}_I$. At the left crack tip, the physically inadmissible negative $\widehat{K}_I$ values for all crack lengths considered are predicted for cracks oriented in the intervals $-70^\circ < \theta < 0^\circ$ and $45^\circ < \theta < 90^\circ$. It is of interest to observe that while $\widehat{K}_I$ is predicted to be negative at the left crack tip in the above crack orientation ranges, the same SIF component is also predicted to be negative at the corresponding right crack

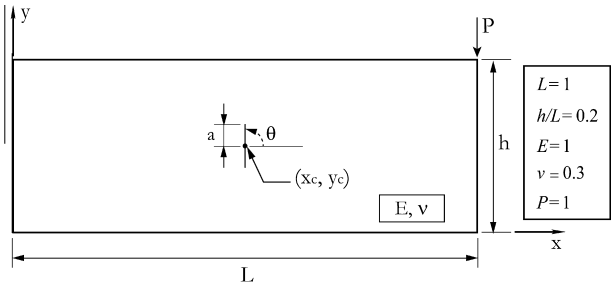

Fig. 13. Schematic showing the fundamental parameters involved in the crack orientation parametric study. The crack location is at the domain center while the study is conducted for four different crack lengths, i.e. $l/L = 2a/L = 0.03,\ 0.05,\ 0.07,\ 0.10$. The results reported in Figs. 14 and 15 were obtained under plane strain condition.

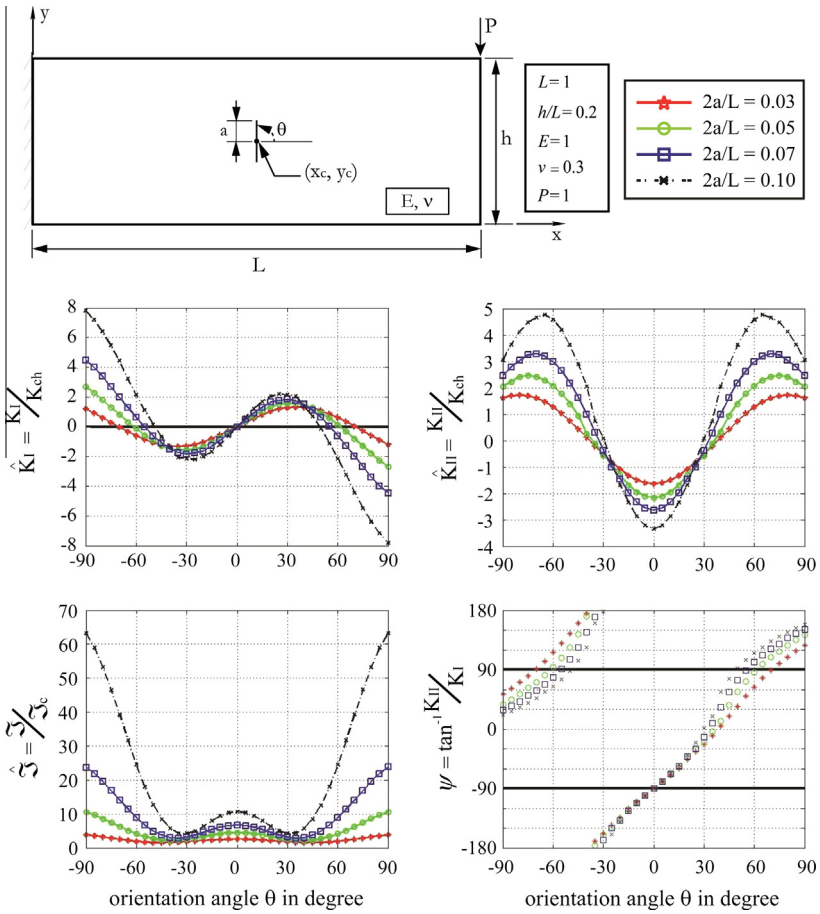

Fig. 14. Simulation predictions for the non-dimensional energy release rate, Mode I, Mode II SIF components and mode mixity at the left crack tip, obtained under plane strain condition. The simulations were carried out for a beam of aspect ratio $h/L = 0.2$ with a sharp crack centered at the middle of the beam domain. The crack orientation angle θ was varied in the range of -90° to $+90^\circ$ with increment of $+5^\circ$ between successive models. Results are reported for four different non-dimensional crack lengths, i.e. $l/L = 2a/L = 0.03, 0.05, 0.07, 0.10$. The simulations were conducted assuming linear elastic and isotropic material response.

tip as shown in Fig. 15. This observation implies that the orientation of a fully embedded crack in the cantilever beam system under consideration plays a key role on whether the crack will remain fully closed, partially closed or fully open during loading. Linearity also implies that such effects would reverse upon reversal of the direction of the applied loading. Thus, when crack surface closure is predicted for a statics case, one would need to be mindful of the non-linear contact effects that definitely would come into play during an oscillatory applied load or when performing modal and frequency response analysis.

It is again of interest to observe that $\widehat{K}_I$ at the right crack tip remains positive for all crack lengths considered when $0^\circ < \theta < 90^\circ$ whereas crack closure is predicted at the left crack tip when $45^\circ < \theta < 90^\circ$.

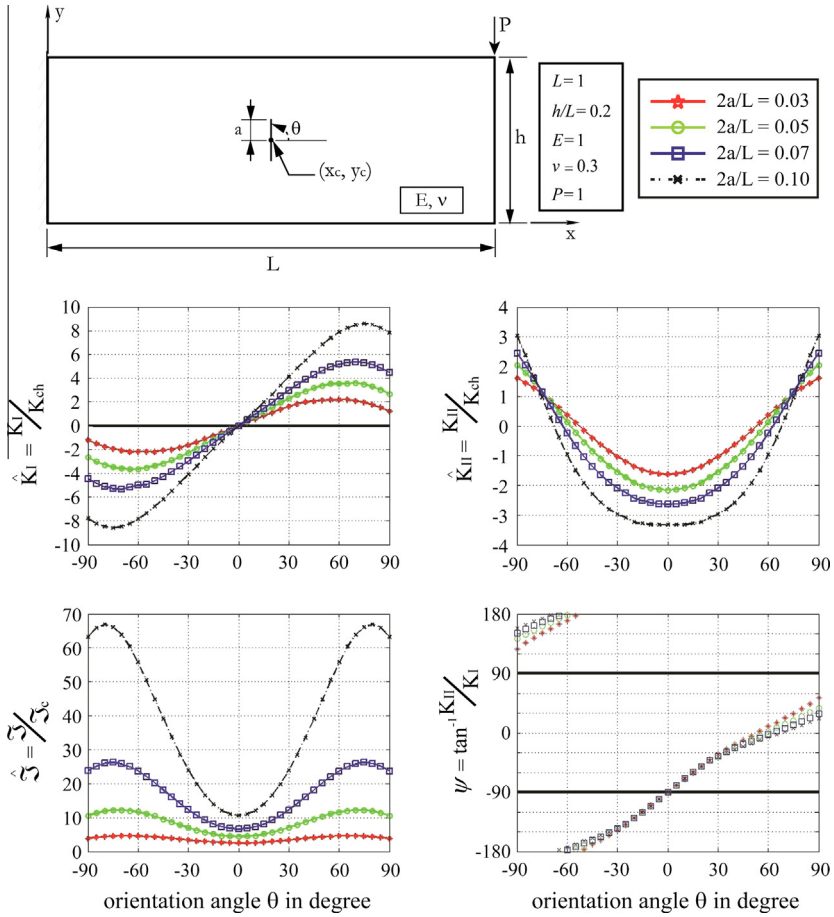

Fig. 15. Simulation predictions for the non-dimensional energy release rate, Mode I, Mode II SIF components and mode mixity at the right crack tip, obtained under plane strain condition. The simulations were carried out for a beam of aspect ratio $h/L = 0.2$ with a sharp crack centered at the middle of the beam domain. The crack orientation angle θ was varied in the range of -90° to $+90^\circ$ with increment of $+5^\circ$ between successive models. Results are reported for four different non-dimensional crack lengths, i.e. $l/L = 2a/L = 0.03,\ 0.05,\ 0.07,\ 0.10$. The simulations were conducted assuming linear elastic and isotropic material response.

While using linear theory physically inadmissible $\widehat{K}_I$ values are predicted for certain crack orientation ranges for both the left and right crack tips, no such inadmissible results are predicted for the $\widehat{K}_{II}$ SIF components dominating the left and right crack tip regions. As shown in Figs. 14 and 15, appreciable non-dimensional $\widehat{K}_{II}$ estimates are predicted for both crack tips. As discussed earlier in this study, the Mode I SIF vanishes at $\theta = 0^\circ$, i.e. for horizontal cracks, while the Mode II SIF component acquires a local maximum in its absolute value for both the left and right crack tips for all crack lengths considered. This finding further reinforces the previous observations that a fully embedded horizontal crack in a cantilever beam under end force loading behaves like a pure Mode II crack. This finding is utilized elsewhere [24] along with beam curvature findings in obtaining analytical estimates of the near-tip energy release rate using J-integral approach. In those studies, a four beam model is developed which includes rotational springs at the crack tip regions as needed to account for the increased compliance induced by the presence of the horizontal crack. Particularly, as described above, a four beam model including rotational springs at the crack tip regions is developed to account for the effects on the structural compliance with the presence of the embedded horizontal crack. The rotary spring stiffnesses are calculated using the known J-integral and are expressed in terms of the beam geometry, crack center location and crack length. Once established, beam frequencies and mode shapes can be calculated. Frequency shifts from that of the healthy beam can then be used to guide a crack detection algorithm as discussed elsewhere [24,31].

It is also of interest to observe that these linear theory results suggest that an intricate interplay exists between the two stress intensity factor components dominating either the left or right crack tip regions. More specifically, it appears from the profiles shown in Figs. 14 and 15, that a crack oriented in such a way that its Mode I component vanishes, then its Mode II component acquires a local extreme and vice versa. Such a finding may provide new and novel approaches in developing analytical models for such systems as needed to better understand the mechanics of beams with fully embedded cracks such as the system under consideration.

6. Conclusions

In this work, a cantilever beam with an embedded sharp crack and subjected to a transverse end loading has been modeled using linear finite elements. Dedicated mapped meshing, pre-processing, processing and post-processing algorithms aimed at conducting broad parametric studies have been developed and integrated into a specialized analysis algorithm. Non-dimensional FE models were developed and used to study the effects of crack length, crack orientation, and crack location, on the near-tip fracture characteristics, such as energy release rate, Mode I and Mode II stress intensity factors, and associated mode mixity. Over 2000 non-dimensional finite element models for beams with fully embedded cracks have been used in conducting the reported parametric studies.

It has been demonstrated through the above simulations that a fully embedded crack in the beam under consideration is subjected to mixed mode fracture conditions with the exception of a horizontal crack. Broad regions of physically inadmissible crack surface interpenetrations are predicted for both the left and right crack tip regions for non-horizontal cracks. Such physically inadmissible effects are predicted in the current study due to the assumption of linearity which does not allow for crack closure effects. Again through the reported parametric studies, it has been established that physically admissible near tip Mode I and Mode II stress intensity factors grow or decrease monotonically with crack length. The study also revealed that the horizontal crack behaves more like a pure Mode II crack regardless of its location in the beam. Such observations are utilized in setting up subsequent and relevant studies on exploring the effects of a horizontal crack on the deflection, slope and curvature of the cracked beam. The findings of this study form the foundation for the development of effective non-model based crack and damage detection methodologies.

Acknowledgements

Support for this work was provided by the University of Maryland, Baltimore County (UMBC), Designated Research Initiative Fund (DRIF), the UMBC Graduate School through a Dissertation Fellowship and the Mechanical Engineering Department at UMBC through Graduate Teaching Assistantship funds.

References

[1] Doyle MW, Stanley EH, Havlick DG, et al. Aging infrastructure and ecosystem restoration. Science 2008;319:286–7.
[2] Doebling SW, Farrar CR, Prime MB. Summary review of vibration-based damage identification methods. Shock Vibr Digest 1998;30(2):91–105.
[3] Dimarogonas AD. Vibration of cracked structures: a state of the art review. Engng Fract Mech 1996;55(5):831–57.
[4] Salawu OS. Detection of structural damage through changes in frequency: a review. Engng Struct 1997;19(9):718–23.
[5] Chondros TG, Dimarogonas AD. Vibration of a cracked cantilever beam. J Vib Acoust 1998;120(3):742–6.
[6] Nandwana BP, Maiti SK. Modeling of Vibration of beam in presence of inclined edge or internal crank for its possible detection based on frequency measurements. Engng Fract Mech 1997;58(3):193–205.
[7] Ostachowicz WM, Krawczuk M. Analysis of the effect of cracks on the natural frequencies of a cantilever beam. J Sound Vib 1991;150(2):191–201.
[8] Rizos PF, Aspragathos N, Dimarogonas AD. Identification of crack location and magnitude in a cantilever beam from the vibration modes. J Sound Vib 1990;138(3):381–8.
[9] Pandey AK, Biswas M, Samman MM. Damage detection from changes in curvature mode shapes. J Sound Vib 1991;145(2):321–32.
[10] Rice JR. A path independent integral and the approximate analysis of strain concentration by notches and cracks. J Appl Mech 1968;35:379–86.
[11] Ioakimidis NI. Locating a crack of arbitrary but known shape by the method of path-independent integrals. Int J Solids Struct 1993;30(14):1939–56.
[12] Lei Y. J-integral and limit load analysis of semi-elliptical surface cracks in plates under tension. Int J Press Vessels Pip 2004;81(1):21–30.
[13] Lei Y. J-integral and limit load analysis of semi-elliptical surface cracks in plates under bending. Int J Press Vessels Pip 2004;81(1):31–41.
[14] Lei Y. J-integral and limit load analysis of semi-elliptical surface cracks in plates under combined tension and bending. Int J Press Vessels Pip 2004;81(1):43–56.
[15] Rice JR, McMeeking RM, Parks DM. Recent finite element studies in plasticity and fracture mechanics. Comput Methods Appl Mech Engng 1979;17–18(2):411–42.
[16] Charalambides PG, McMeeking RM. Near-tip mechanics of stress-induced microcracking in brittle materials. J Am Ceram Soc 1988;71(6):465–72.
[17] Matos PPL, McMeeking RM, Charalambides PG, Drory MD. A method for calculating stress intensities in bimaterial fracture. Int J Fract 1989;40:235–54.
[18] Charalambides PG, Zhang W. An energy method for calculating the mixed mode stress intensities in orthotropic bimaterial fracture. Int J Fract 1996;76:97–120.
[19] Skrinar M. Elastic beam finite element with an arbitrary number of transverse cracks. Finite Elem Anal Des 2009;46(3):181–9.
[20] Potirniche GP, Hearndon J, Daniewicz SR, et al. A two-dimensional damaged finite element for fracture applications. Engng Fract Mech 2008;17(13):3895–908.
[21] Hall KJ, Potirniche GP. A three-dimensional edge-crack finite element for fracture mechanics applications. Int J Solids Struct 2012;49(2):328–37.
[22] Sancho JM, Planas J, Cendon DA, et al. An embedded crack model for finite element analysis of concrete fracture. Engng Fract Mech 2007;74(1–2):75–86.
[23] Charalambides PG, Kuhn JL. A guide to finite element modeling. Baltimore, MD: The University of Maryland, Baltimore County; 1999.
[24] Fang X. The mechanics of an elastically deforming cantilever beam with an embedded sharp crack and subjected to an end transverse loading. (Doctoral dissertation). Retrieved from ProQuest Dissertations and Theses (Publication No. 3609879); 2013.
[25] Broek D. Elementary engineering fracture mechanics. New York, NY: Springer Press; 1974.
[26] Kanninen MF, Popelar CH. Advanced fracture mechanics. New York, NY: Oxford Press; 1986.
[27] Irwin G. Analysis of stresses and strains near the end of a crack traversing a plate. J Appl Mech 1957;24:361–4.
[28] Parks DM. A stiffness derivative finite element technique for determination of elastic crack tip stress intensity factors. Int J Fract 1974;10(4):487–502.
[29] Parks DM. The virtual crack extension method for nonlinear materials behavior. Comput Methods Appl Mech Engng 1977;12:353–64.
[30] Charalambides PG, Lund J, Evans AG, McMeeking RM. A test specimen for determining the fracture resistance of bimaterial interfaces. J Appl Mech 1989;56:77–82.
[31] Aladiev V. Damage and crack detection methods based on the vibrational characteristics of damaged and cracked cantilever beams (Doctoral dissertation). Retrieved from ProQuest Dissertations and Theses (Publication No. 3609817); 2013.